

Determination of critical resolved shear stresses associated with $\langle a \rangle$ slips in pure Zn and Zn-Ag alloys via micro-pillar compression

Wiktor Bednarczyk^{a,1,*}, Maria Wątroba^{b,1,*}, Manish Jain^{b,c}, Krzysztof Mech^d, Piotr Bazarnik^a, Piotr Bała^{d,e}, Johann Michler^b, Krzysztof Wiecezrak^b

^a Warsaw University of Technology, Faculty of Materials Science and Engineering, Wołoska 141, 02-507 Warsaw, Poland

^b Empa, Swiss Federal Laboratories for Materials Science and Technology, Laboratory of Mechanics of Materials and Nanostructures, CH-3602 Thun, Feuerwerkerstrasse 39, Switzerland

^c School of Mechanical and Manufacturing Engineering, University of New South Wales (UNSW Sydney), Sydney, NSW 2052, Australia

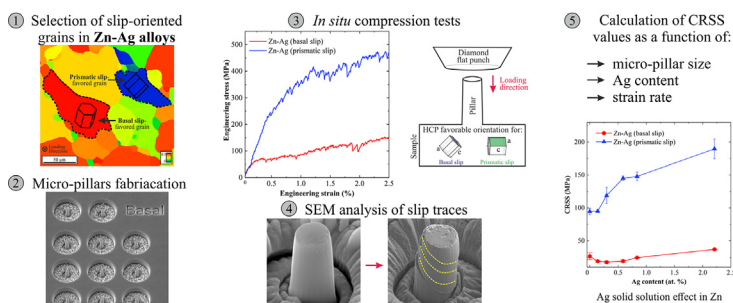
^d AGH University of Science and Technology, Academic Centre for Materials and Nanotechnology, Al. A. Mickiewicza 30, 30-059 Krakow, Poland

^e AGH University of Science and Technology, Faculty of Metals Engineering and Industrial Computer Science, Al. A. Mickiewicza 30, 30-059 Krakow, Poland

HIGHLIGHTS

- For the first time, critical resolved shear stresses in Zn and Zn-Ag alloys were measured using micro-pillar compression.
- Reducing micro-pillar diameter from 9 to 3 μm increases shear stress from 11.3 to 26.6 MPa in the basal slip system.
- The Ag solid solution increases shear stresses more effectively in the prismatic slip than in the basal slip systems.
- Dislocation starvation governs the deformation in dislocation-free 3 μm Zn micro-pillars favorably oriented for basal slip.

GRAPHICAL ABSTRACT



ARTICLE INFO

Article history:

Received 29 November 2022

Revised 4 March 2023

Accepted 31 March 2023

Available online 7 April 2023

Keywords:

Zinc alloys

Micro-pillar compression

Critical resolved shear stress

Solid-solution strengthening

ABSTRACT

The room-temperature plastic deformation behavior of pure Zn and Zn-Ag (0–2.2 at.%) biodegradable alloys has been investigated via uniaxial *in situ* micro-pillar compression tests performed within a scanning electron microscope. The critical resolved shear stresses (CRSS) were quantified as a function of micro-pillar diameter. The compression of single crystal micro-pillars was performed at various strain rates in carefully selected grains, the crystallographic orientation of which facilitates deformation either via basal $\{0001\}\langle 11\bar{2}0 \rangle$ or prismatic $\{10\bar{1}0\}\langle 11\bar{2}0 \rangle$ slip. The CRSS values increased with decreased micro-pillar diameter, revealing a more pronounced size effect in pure Zn deformed via basal slip. The observed solid solution strengthening effect in Zn-Ag alloys with increasing Ag content was associated with a CRSS increase from 26.6 MPa to 37.0 MPa (by $\sim 40\%$) in the basal slip system and from 99.1 MPa to 188.4 MPa (by $\sim 104\%$) in the prismatic slip system. The extraordinarily high CRSS values for basal slip activated in pure Zn and Zn-0.14Ag alloy compared to the solid solution strengthening model was attributed to the critically low dislocation density. In the Zn-Ag alloy with Ag content > 0.5 at.% higher dislocation densities are expected, which result in a more predictable plastic deformation behavior.

© 2023 The Author(s). Published by Elsevier Ltd. This is an open access article under the CC BY license (<http://creativecommons.org/licenses/by/4.0/>).

* Corresponding authors.

E-mail addresses: wiktor.bednarczyk@pw.edu.pl (W. Bednarczyk), maria.watroba@empa.ch (M. Wątroba).

¹ These authors contributed equally to this work.

1. Introduction

In recent years Zn and Zn alloys have gained tremendous interest as a new class of bioresorbable metallic materials due to their promising biodegradation behavior and biocompatibility. Nevertheless, insufficient mechanical strength and low ductility of pure Zn inhibit its application for load-bearing medical devices, such as cardiovascular stents, orthopedics implants, wound closures, etc. [1]. To meet the mechanical requirements of such applications, works studying the effect of alloying on Zn's plastic deformation behavior are ongoing [2,3]. Additionally, in the context of medical implant applications, the biological behavior of Zn can be tailored via alloying. One candidate that enhances the strength and ductility of Zn, as well as provides antimicrobial properties and low cytotoxicity, is silver [4,5]. Furthermore, the corrosion rates of Zn-Ag-based alloys can be tuned by means of thermomechanical processing, while ensuring uniform biodegradation [6,7].

In principle, Zn's brittleness and poor cold workability originate from its hexagonal close-packed (HCP) crystal structure and the limited number of slip systems, making it difficult to be plastically deformed at low temperatures. A high c/a lattice ratio (1.856) in Zn causes strong anisotropy of its mechanical behavior. The Zn structure possesses one close-packed plane (basal plane), which contributes to substantial differences in critical resolved shear stress (CRSS) for different slip systems [8]. CRSS is a combination of the Peierls-Nabarro stress and all hardening mechanisms present in a material. It is defined as a shear stress component, resolved in the direction of slip, necessary to initiate slip within a grain. Therefore, being able to follow the CRSS phenomenon is crucial in understanding a material's plasticity. Among four slip systems available in Zn: basal $\langle a \rangle$, prismatic $\langle a \rangle$, pyramidal $\langle a \rangle$ and pyramidal $\langle c + a \rangle$, the basal slip, possessing the lowest CRSS, is generally the easiest to activate during deformation. According to reports concerning CRSS in Zn, non-basal slip or twin systems have at least one order of magnitude higher CRSS than that determined for the basal slip system [9–13], with the $\text{CRSS}_{\text{basal}}:\text{CRSS}_{\text{prism}}:\text{CRSS}_{\text{pyr}}:\text{CRSS}_{\text{twinning}}$ ratio amounting to approx. 1:15:10:30 [14].

The mechanical properties of bulk Zn measured at the macro-scale are affected by microstructural features of the polycrystalline sample. These include grain size, type of alloying elements, presence of second phases, initial crystallographic texture, and type and the fraction of grain boundaries. Furthermore, loading direction, strain rate, temperature, activated deformation mechanisms and corresponding CRSS play a major role in the stress-strain response. The number of factors that simultaneously influence the deformation process complicates the analysis of individual strengthening mechanisms and the characterization of mechanical properties-microstructure relations. Therefore, micromechanical testing methods can be beneficial in distinguishing the contribution of several single mechanisms in the total Zn strengthening effect. *In situ* micro-pillar compression tests have recently gained increasing attention as a powerful tool for quantifying the uniaxial mechanical response and characterizing the stress-strain behavior related to individual deformation modes at small-length scales. In addition, it allows for measuring the CRSS for a particular slip or twinning mode (according to the Schmidt law) under different loading conditions. For instance, to activate non-basal slip systems in HCP crystals, the load must be subjected perpendicular or parallel to the basal plane to minimize the Schmidt Factor (SF) for the basal slip and maximize it for the chosen non-basal slip [10,15]. Micro-pillars can be fabricated within a single grain with a well-defined orientation or at the specific grain boundary identified via electron backscattered diffraction (EBSD) in scanning electron microscope (SEM), and its deformation is induced via loading with a flat punch at a selected strain rate and temperature. The use of focused ion beam

(FIB) machining enables serial sample manufacturing, facilitating micromechanical testing of multiple geometries.

Considering the necessity of improving the mechanical properties of Zn alloys to fulfill the criteria for bioresorbable implants, it is essential to quantify the CRSS for more complex Zn-based materials. It has been shown for Mg alloys that solute atoms might play a key role in enhancing the ductility of HCP metals by reducing the difference in the CRSS value between the basal and non-basal slip systems. This is achieved by strengthening the basal slip and/or softening the non-basal slip [16–18]. Moreover, it has been found that solute elements can effectively participate in improving the overall yield strength of Zn [19]. In metallic alloys, the generalized solid solution strengthening model may be presented as:

$$\sigma_{\text{sol}} = A + k_{\text{sol}}^{\frac{1}{n}} \cdot c^n \quad (1)$$

where: A is a material constant, k_{sol} is the solid solution strengthening coefficient (previously calculated for Zn-Ag alloys as $6.6 \text{ MPa} \cdot (\text{at.}\%)^{-1/2}$) [20], c is the element content in at. % and n is a constant equal to $1/2$ [21,22]. Detailed analysis of solid-solution strengthening in polycrystalline materials must consider loading direction and texture effects. However, single-crystalline micro-pillar compression tests allow directly measuring of solid solution strengthening effects on the particular slip system. Silver, which has been found to enhance Zn's mechanical properties, exhibits relatively high solubility in Zn and thus may provide solid solution strengthening [20]. According to the binary system, the maximum solubility of Ag in Zn reaches up to 5 at. % at elevated temperatures. Tailoring the mechanical properties of Zn by alloying is a strategy that requires knowledge of the effect of solute atoms on plastic deformation mechanisms, particularly the CRSS values. Extensive studies on the Ag strengthening effect in Zn-Ag alloys have shown to be related to solid solution formation, grain refinement, and precipitation hardening [23,24]. Therefore, the main advantage of the micromechanical experimental approach is extracting the distinct solid solution effect, which has yet to be fully characterized in Zn-Ag alloys. Moreover, to the best of the authors' knowledge, the effect of any Ag additions on CRSSs has never been studied for Zn alloys, regardless of the applied testing method.

Another investigated phenomenon related to micro-pillar stress-strain behavior is the so-called *size effect*, which has been extensively explored in various FCC and BCC metals, and less so in HCP metals [25–27]. In principle, it was found that the flow stress (σ) at a given plastic strain follows a power-law dependence on micro-pillar diameter (D), within a range of a couple of hundred nanometers to tens of micrometers:

$$\sigma \propto A \cdot D^{-m} \quad (2)$$

where: A is a size effect coefficient, and m is a size exponent [26,28]. Many micro-pillar compression studies follow the idea of "*smaller is stronger*", so as the pillar diameter decreases, the flow stress and strain hardening increase [29]. In HCP metals, the micro-pillar size can also affect the activation or vanishing of twinning during deformation at specific orientations [30].

This work studies the plastic deformation behavior of Zn-Ag samples at room temperature via single crystalline micro-pillar compression as a function of Ag content (pure Zn and Zn-Ag alloys), while aiming to activate individual basal or prismatic slips to evaluate their CRSS values. Additionally, in the context of the applied methodology, the effect of micro-pillar dimensions was examined to most accurately select the experimental conditions. Furthermore, strain rate sensitivity, being an equally important parameter for deformation mechanisms, was characterized. As a result, this work provides CRSS values required for the activation

of $\langle a \rangle$ slips on the $\{0001\}$ basal and $\{10\bar{1}0\}$ prismatic planes in Zn-Ag (0–2.2 at. %) alloys.

2. Experimental materials and procedures

Pure Zn and Zn-Ag alloys were prepared using high-purity Zn (>99.995 wt%) and Ag (>99.995 wt%). Metals were melted in a graphite crucible at 650 °C and cast into a steel mold to achieve a series of Zn-Ag (0–2.2 at. %) alloys. Cast ingots were annealed at 400 °C for 4 h and subsequently water-cooled to obtain a uniform chemical composition. The chemical composition of the investigated alloys was analyzed using a Rigaku ZSX Primus IV wavelength dispersive X-ray fluorescence spectrometer (WD-XRF). Finally, the samples were subjected either to hot channel die pressing or hot extrusion at 300 °C to obtain a favorable texture. Hot processing at 300 °C was sufficient to produce a fully recrystallized, coarse-grained microstructure, while also providing multiple grains to seek the desired orientation for micropillar compression experiments.

Single-slip investigations in polycrystalline samples requires a detailed microstructure analysis by means of EBSD. Samples were cold mounted, ground, and polished using alcohol-based diamond suspensions. The final preparation step was low-angle Ar^+ ion polishing using a Hitachi IM4000Plus Ion Milling System. The EBSD measurements were performed using FEI Versa3D and Tescan Mira scanning electron microscopes (SEM) equipped with EDAX EBSD detectors. The crucial step was identifying grains oriented in two specific directions, in which only basal $\{0001\}\langle 11\bar{2}0 \rangle$ or prismatic

$\{10\bar{1}0\}\langle 11\bar{2}0 \rangle$ slip systems can occur. Fig. 1 presents an overview of the experimental steps required to find grains with a desirable orientation. Activation of a particular slip system was evaluated based on the SF calculation (Fig. 1e). Basal-promoting grains must exhibit an $\text{SF}_{\text{basal}} > 0.45$, while prismatic-susceptible grains must meet the following conditions: $\text{SF}_{\text{basal}} \leq 0.02$ and $\text{SF}_{\text{prism}} \geq 0.47$. To avoid EBSD distortion, each measurement was performed twice, firstly in the form of a coarse EBSD map, and secondly using an EBSD map focused directly on the selected grain.

Micro-pillars with diameters of 3.0 μm , 6.3 μm , and 9.0 μm (further referred to as 3 μm , 6 μm , and 9 μm micro-pillars, respectively) and height to diameter ratio equal to 2.5:1 were fabricated within single grains using a Ga^+ FIB in a dual-beam Tescan Vela FIB-SEM. To reduce the risk of ion milling-induced material deformation [31,32], multi-step milling was performed using the following ion beam currents: 4.5 nA, 1 nA, 160 pA, and 40 pA at 30 kV. After fabrication, the dimensions of each pillar were measured using a Hitachi S-4800 high-resolution cold field emission SEM.

First, *in situ* compression tests were performed inside the SEM chamber of the Philips XL30 ESEM FEG on Zn micro-pillars at a strain rate of 10^{-3} s^{-1} to determine the size effect on CRSS. Additionally, dynamic micro-pillar compression tests at different strain rates were performed on Zn and Zn-Ag alloys to measure the effect of strain rate and Ag additions on the CRSS of individual slip systems. Based on the size effect results, only 3 μm diameter micro-pillars were chosen for further analysis. All tests were performed in displacement control mode, with up to 10 % of deformation at room temperature using a 20 μm diamond flat punch tip installed

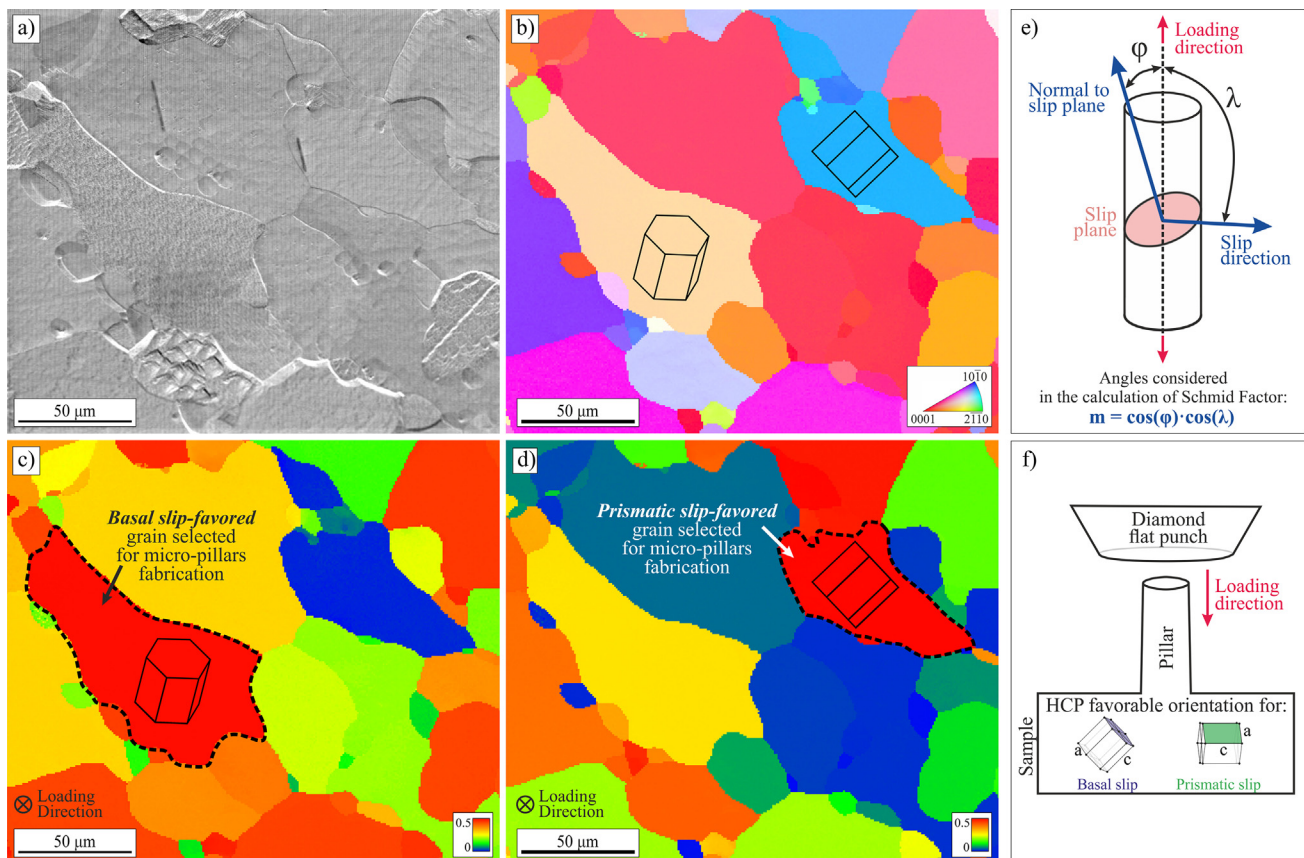


Fig. 1. Overview of the experimental steps necessary to find a grain promoting the activation of basal or prismatic slip during deformation: SEM-SE image (a); EBSD-IPF map (b); SF map for the basal slip system (c); SF map for the prismatic slip system (d). Angles considered during Schmid Factor calculations (e); Schematic of the *in situ* micro-pillar compression tests (f).

in an Alemnis Standard Assembly *in situ* nanoindenter. At least three compression tests were performed under each condition to ensure repeatability. After deformation, images from two perpendicular directions were collected to observe traces of deformation slip on each micro-pillar. Moreover, post-deformation EBSD analysis was performed on the cross-sections of pure Zn micro-pillars of varying diameters. Firstly, the deformed pillars were coated with a protective W layer, after which they were coarse ion-milled (30 kV, 1 nA), transferred to Cu lift-out grids, and finally ion-polished using low-voltage, low-current FIB conditions (5 kV, 30 pA). The EBSD measurements were performed in reflection mode at 20 kV, with a step size of 40 nm.

3. Results

3.1. Effect of micro-pillar diameter on CRSS in pure Zn

The effect of pillar size on CRSS and the deformation behavior in pure Zn was investigated in basal and prismatic $\langle a \rangle$ slip systems via compression tests at a strain rate of 10^{-3} s^{-1} . Fig. 2a presents the initial stage of compression stress–strain curves of basal-favor-oriented pillars. Reduction in micro-pillar diameter resulted in a significant increase in yield stress. Moreover, a significant difference in flow behavior was observed. Micro-pillars with a diameter of 9 μm present minor stress drops during straining and a negligible strain hardening effect. The ratio of flow stress at 2 % of deformation to yield stress ($\sigma_{2\%}/\sigma_{YS}$) equals 1.09 in micro-pillars with a diameter of 9 μm . Reduction in micro-pillar diameter to 6 μm and 3 μm changed the strain hardening ratio to 0.93 in both cases. Therefore, the overall strain hardening effect was negative, however, the event of short-term significant strengthening followed by instantaneous stress drops to the initial level repeatedly occurred. A different behavior was observed in the prismatic slip system, presented in Fig. 2b. The micro-pillar diameter effect on strength is less prominent than in the basal slip system. However, the observed strain hardening was equal to 1.68 in 9 μm micro-pillars, and 1.73 in the 6 μm and 3 μm cases.

To evaluate a size effect in micro-pillars of Zn deformed via basal and prismatic slip, the CRSS was calculated following the Schmid law:

$$\text{CRSS} = \sigma_{YS} \cdot m \quad (3)$$

where: σ_{YS} is the yield stress determined from the stress–strain curve, and m is the Schmidt factor corresponding to the single slip system. It was found that the CRSS value, at which a slip would occur, was constant for samples with specific dislocation densities and purities. To move dislocations, a particular stress σ_{YS} must be applied to overcome resistance to dislocation motion and initiate slip in a grain. With this in mind, the CRSS values were correlated with pillar diameters, based on the stress–strain curves and SF values (Fig. 2c). It can be seen that the diameter of the micro-pillar significantly influenced the obtained CRSS. For example, for a diameter of 3 μm , the CRSS in the basal slip system (CRSS_B) equaled 26.6 MPa, while a decrease in CRSS_B occurred when increasing the diameter to 6 μm (16.8 MPa) and 9 μm (11.3 MPa). A similar but relatively less significant effect occurred for the prismatic slip system (CRSS_P), where 99.1 MPa was obtained for a diameter of 3 μm , while for 9 μm , 81.8 MPa.

Fig. 3 presents images of micro-pillars with different diameters after deformation at a strain rate of 10^{-3} s^{-1} . The micro-pillars' deformation behavior depends on the type of slip system, but not on their diameter. For example, deformation in the basal slip system generated parallel, narrow slip traces. For 3 μm micro-pillars (Fig. 3) these traces as distinctly separated from one another across the entire pillar, whereas for 6 and 9 μm micro-pillars, they are

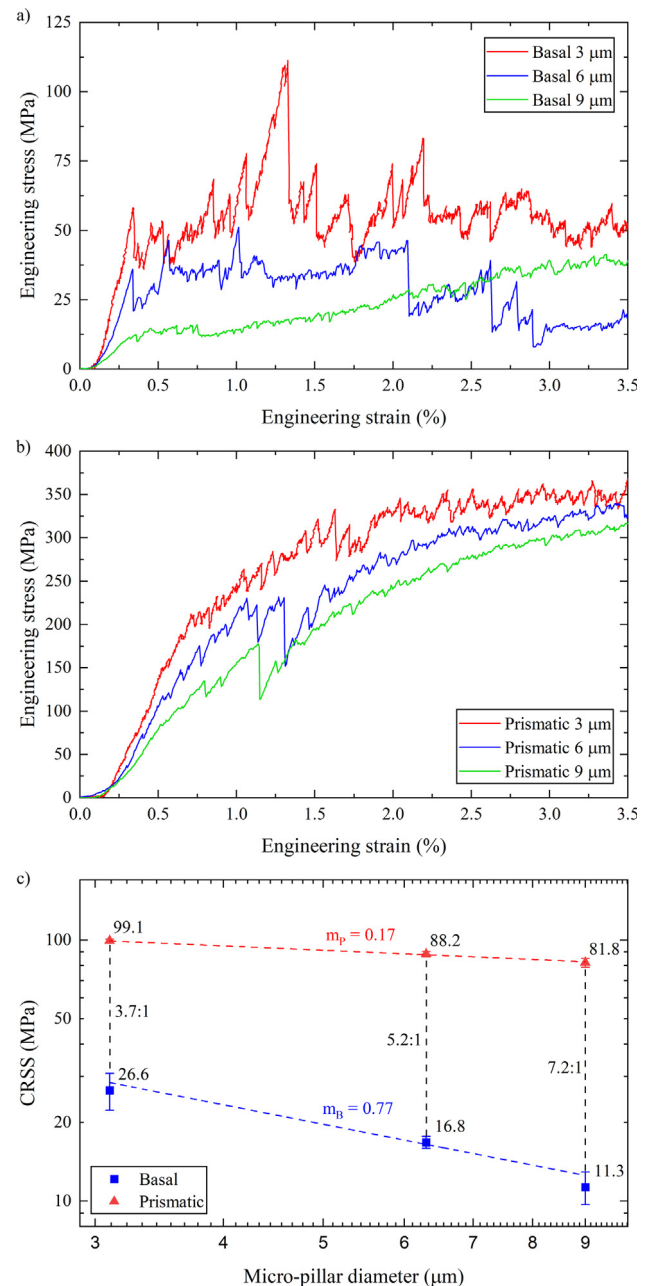


Fig. 2. Compression stress–strain curves of pure Zn, with varying micro-pillar diameter, deformed in (a) basal slip system and (b) prismatic slip system. (c) The effect of micro-pillar diameter on CRSS in basal and prismatic slip systems and $\text{CRSS}_P/\text{CRSS}_B$ ratio in pure Zn at a strain rate of 10^{-3} s^{-1} .

more localized (Fig. 3c and d). Characterizing the deformation in the prismatic slip system proved to be more challenging. The slip traces were blurred and barely visible. Nevertheless, it was possible to distinguish two slip planes on the 3 μm micro-pillars (Fig. 3), while only one can be seen for the larger-diameter pillars (Fig. 3f and g).

SEM observations of deformed pillars are insufficient to comprehensively describe the deformation mechanisms. Therefore, an EBSD analysis was performed on cross-sections of the deformed micro-pillars, parallel to the compression axis. Fig. 4 presents inverse pole figure maps superimposed on image quality maps (IPF + IQ), Kernel average misorientation maps (KAM), and Schmid Factor maps (SF) for the studied basal and prismatic slip systems. The results show a uniform orientation within the basal slip-favored micro-pillars, except for the ones with the largest diame-

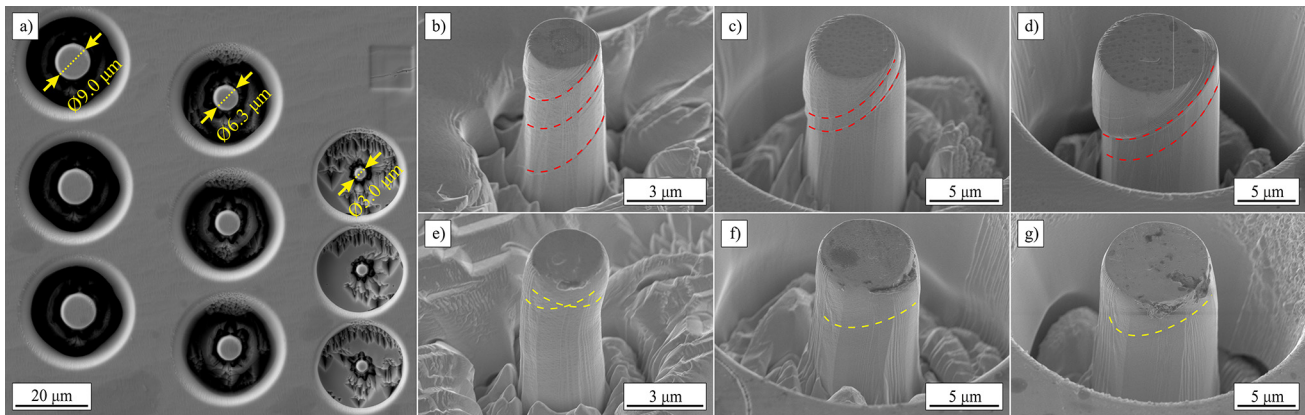


Fig. 3. SEM images of non-deformed (a) and deformed pillars in basal (b–d) and prismatic (e–g) slip systems. Micro-pillar diameters: 3 μm (b,e), 6 μm (c,f), and 9 μm (d,g).

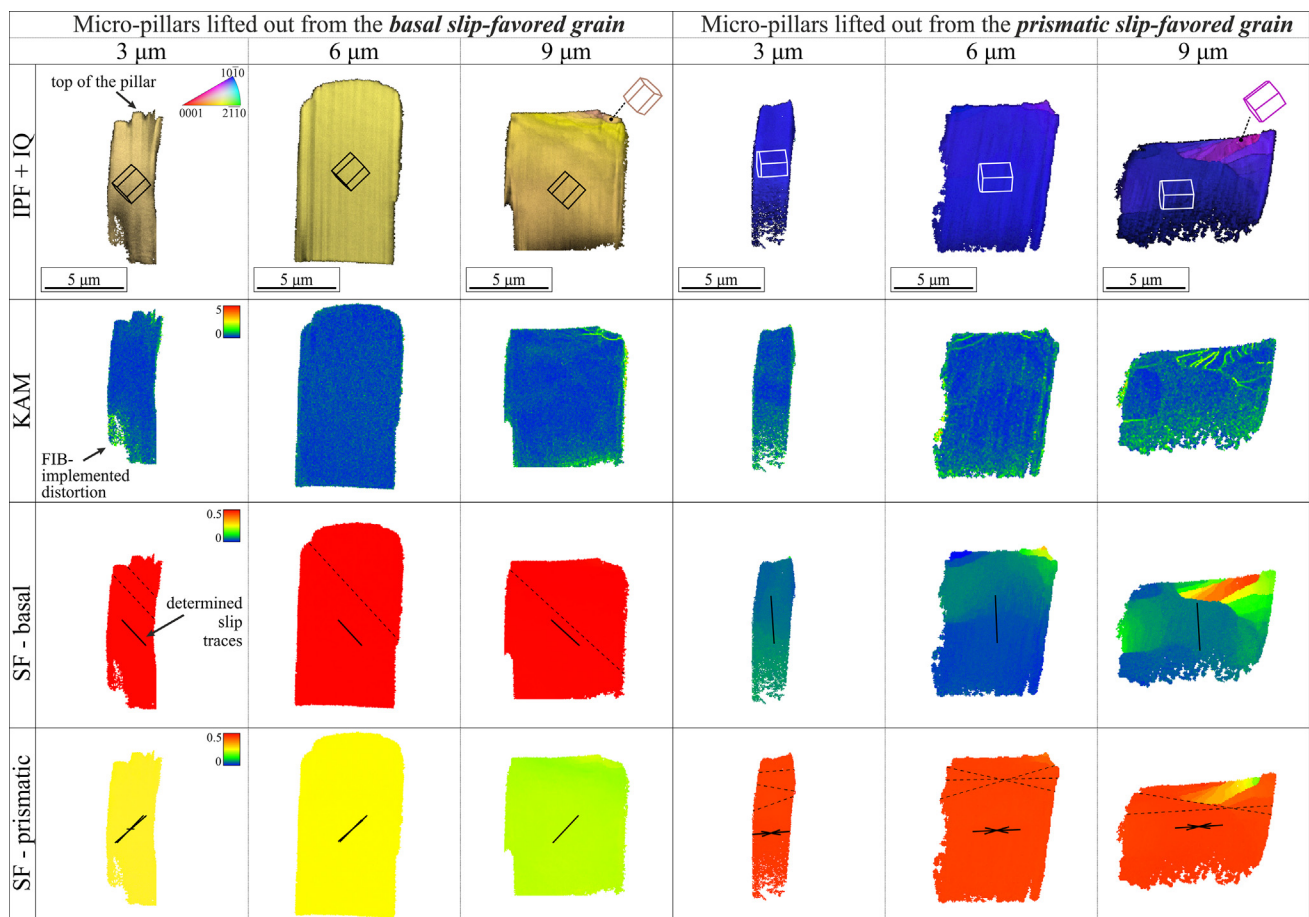


Fig. 4. Cross-sectional EBSD analysis of deformed micro-pillars in basal and prismatic slip systems, with diameters of 3 μm , 6 μm , and 9 μm . From the top: inverse pole figure maps superimposed on image quality maps (IPF + IQ), Kernel average misorientation maps (KAM), Schmid factor maps in the basal slip system (SF-basal), and Schmid factor maps in the prismatic slip system (SF-prismatic).

ters. Furthermore, no localized misorientation occurred, despite the slip plane crossing the observed slices. A pure shear deformation effect is visible in 6 μm micro-pillars, where the observed deformation plane is almost parallel to the measured basal slip plane. Within the deformed 9 μm micro-pillar, a localized deformation occurred at its top due to initial tip-pillar misalignment. Furthermore, the shading of the IQ map indicate shearing through the basal plane in the largest micro-pillar.

Deformation of the prismatic slip-favored micro-pillars exhibited a higher dependence on micro-pillar diameter than the in

the case of the basal slip-favored ones (Fig. 4). Uniform deformation occurred in 3 μm micro-pillar, where 10 % deformation did not cause any significant lattice rotation. Only a tiny, local fluctuation in KAM value can be observed with height changes of the 3 μm pillar. The deformation behavior of the 6 μm micro-pillars changed, where localized deformation occurred on the top of the pillar, resulting in considerable lattice rotation to a basal-favor orientation.

The KAM and basal SF maps show localized deformation aligned parallel to the determined prismatic slip planes, indirectly con-

firming deformation through an intended prismatic slip system. An increase in a pillar diameter to 9 μm resulted in continuous deformation behavior changes. Compression to 10 % caused a significant lattice rotation to basal-favor orientations. Moreover, major misorientation substructures were formed in an excellent arrangement to predicted prismatic slip planes.

3.2. Effect of Ag content on CRSS in Zn-Ag alloys

The chemical composition of the investigated alloys is presented in Table 1. Pure Zn and low-alloyed Zn-Ag alloys were prepared to analyze the effect of Ag solid solution strengthening. A silver alloying range from 0.14 to 0.59 at. % was selected to focus on single-phase alloys, while greater additions of 0.84 and 2.21 at. % was chosen to produced super-saturated materials.

Fig. 5a presents the initial stage (up to 2.5 % of engineering strain) of compression stress-strain curves of the investigated materials in a basal-favor orientation. Pure Zn and Zn-Ag alloys with Ag additions up to 0.30 at. % exhibited a low strain hardening response, while a further increases in Ag content enhanced the strain hardening value in the basal slip system. The ratio of flow stress at 2 % of deformation to yield stress ($\sigma_{2\%}/\sigma_{YS}$) is presented in Fig. 6, and it equaled 0.93, 1.12, 1.18, 1.40, 1.36, and 1.85 for pure Zn, Zn-0.14Ag, Zn-0.30Ag, Zn-0.59Ag, Zn-0.84Ag, and Zn-2.21Ag, in basal slip, respectively. An opposite effect of Ag content on strain hardening occurred in the prismatic slip system (Figs. 5b and 6). Initially, up to 0.59 at. % of Ag, $\sigma_{2\%}/\sigma_{YS}$ fluctuated around 1.7 while higher Ag concentrations reduced $\sigma_{2\%}/\sigma_{YS}$ to 1.36 for both 0.84 at. % and 2.21 at. % of Ag.

The effect of Ag on the strengthening of basal and prismatic slip systems was directly compared using CRSS values calculated according to Eq. (3). Fig. 7a presents the effect of Ag addition on CRSS_B at various strain rates. Strain rates from 10^{-4} s^{-1} to 10^{-2} s^{-1} do not strongly affect the CRSS value since the measured differences are smaller than the measurement uncertainty. Thus, for a more straightforward interpretation, further analysis will be provided only for a strain rate of 10^{-3} s^{-1} . Regardless of the applied strain rate, the Ag additions caused significant changes in CRSS_B. The measured CRSS_B of pure Zn equaled $26.6 \pm 5.2 \text{ MPa}$. Unexpectedly, minor Ag additions decreased the calculated CRSS_B by approx. 30 %, to $18.9 \pm 1.2 \text{ MPa}$ and $17.5 \pm 1.2 \text{ MPa}$ for Zn-0.14Ag and Zn-0.30Ag alloys, respectively. With further Ag content increases, the CRSS_B increased to $19.1 \pm 2.0 \text{ MPa}$, $24.4 \pm 0.4 \text{ MPa}$, and $37.0 \pm 0.6 \text{ MPa}$ for the Zn-0.59Ag, Zn-0.84Ag, and Zn-2.21Ag alloys, respectively.

Fig. 7b presents a slightly different effect of Ag content on CRSS_P than on CRSS_B. For pure Zn and Zn-0.14Ag alloy, CRSS_P equals $98.9 \pm 3.0 \text{ MPa}$ and $90.5 \pm 5.6 \text{ MPa}$, respectively. A significant increase in CRSS_P value to $117.9 \pm 13.1 \text{ MPa}$, $130.0 \pm 1.9 \text{ MPa}$, and $141.8 \pm 2.6 \text{ MPa}$, occurs for Zn-0.30Ag, Zn-0.59Ag, and Zn-0.84Ag, respectively. An even more prominent increase in CRSS_P to $188.4 \pm 0.5 \text{ MPa}$ was measured for the Zn-2.21Ag alloy. In contrast to the basal slip system, above 0.59 at. % Ag content, the strain rate effect became more remarkable, while it did not play a significant role up to 0.30 at. % of Ag additions. For the Zn-2.21Ag alloy, CRSS_P equals $157.7 \pm 3.7 \text{ MPa}$ and $189.6 \pm 15.0 \text{ MPa}$ at strain rates of 10^{-4} s^{-1} and 10^{-2} s^{-1} , respectively.

Representative SEM images of deformed pillars in basal (top row) and prismatic (bottom row) slip systems are shown in

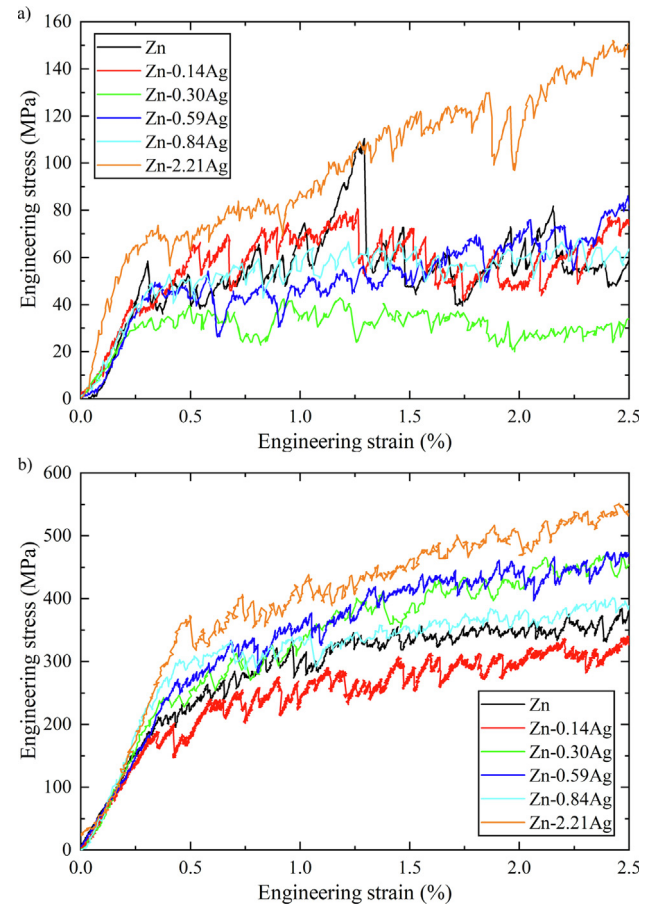


Fig. 5. Compression stress-strain curves of pure Zn and Zn-Ag alloys deformed in (a) basal and (b) prismatic slip systems at a strain rate of 10^{-3} s^{-1} .

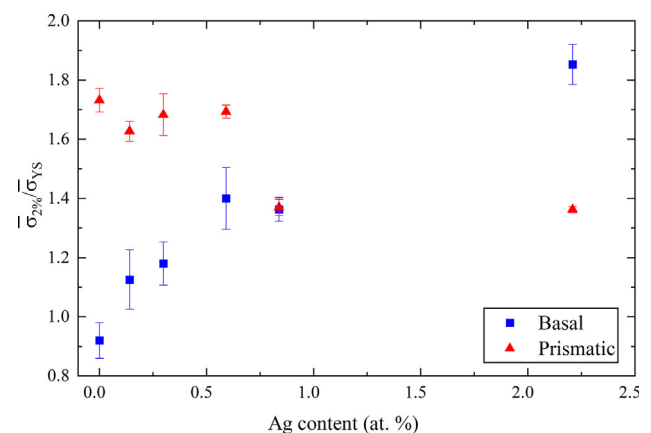


Fig. 6. The effect of Ag content on the $\sigma_{2\%}/\sigma_{YS}$ ratio in basal and prismatic slip systems.

Fig. 8. It is assumed that the specimens showed similar plastic deformation behavior in both slip systems regardless of the applied strain rate. Therefore, in Fig. 8, only micro-pillars deformed at 10^{-3} s^{-1}

Table 1
Measured chemical composition of the investigated alloys.

Alloy	Zn	Zn-0.14Ag	Zn-0.30Ag	Zn-0.59Ag	Zn-0.84Ag	Zn-2.21Ag
Ag content (at. %)	0	0.14	0.30	0.59	0.84	2.21
Ag content (wt. %)	0	0.23	0.49	0.97	1.38	3.59

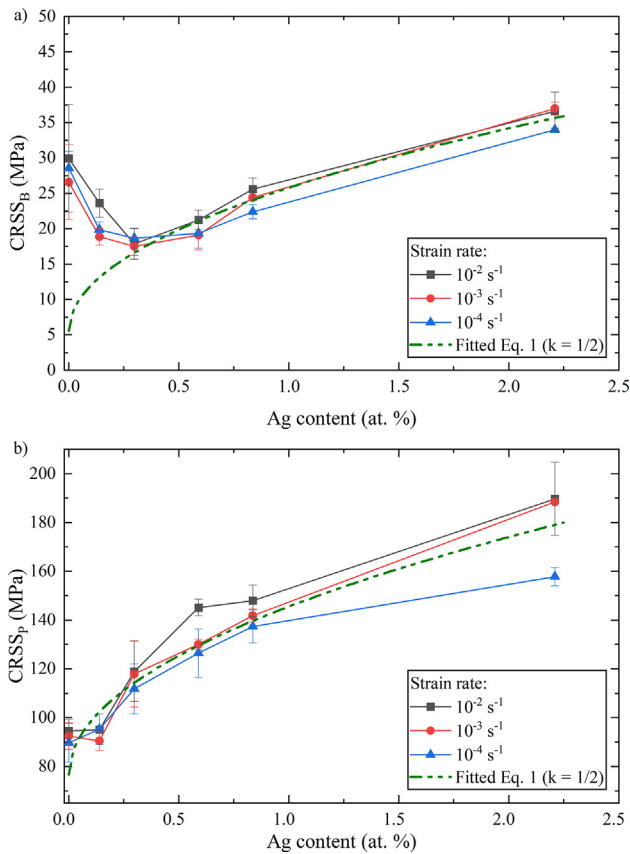


Fig. 7. The effect of Ag content on the CRSS in basal (a) and prismatic (b) slip systems at various strain rates.

s^{-1} were shown. The observed deformation behavior of all investigated samples, i.e. from pure Zn to Zn-2.21Ag, is typical for basal and prismatic slip systems. The basal slip deformation effect appeared as parallel slip plane traces inclined by approx. $40^\circ \div 50^\circ$ to the compression axis. Furthermore, the deformation tended to shear through the entire pillar without any disruptions. The Ag additions caused a gradual change from a localized deformation in a few narrow slip bands in pure Zn to uniform deformation and numerous slip bands in the Zn-2.21Ag alloy. A different behavior was observed in the prismatic slip system, where shallow slip traces were barely visible. Deformation in the prismatic slip system occurs in two favorable planes resulting in buckling rather than

localized pure shearing. In contrast to the basal slip system, where slip activation is followed by a giant avalanche of dislocations that escape the micro-pillar's surface [27], no large slip traces are visible as a result of the prismatic slip. Similar observations were reported for the deformation of Mg-Zn specimens in non-basal slip systems [17].

4. Discussion

4.1. The effect of pillar diameter on the deformation behavior in pure Zn

A significant size effect on micro-pillar deformation has been widely described in literature [33–35]. Nevertheless, Zn has barely been tested using micromechanics methods [27]. The current study examined the size effect, due to the risk of twinning activation or non-uniform deformation during compression tests. A micro-pillar diameter between $3 \mu\text{m}$ and $9 \mu\text{m}$ was chosen based on our previous studies, as the transition from twinning to dislocation dominant deformation occurred within this grain size range [20,36,37]. Additionally, uniform deformation is required to extract a single slip system behavior in a highly anisotropic Zn crystal [38,39].

As presented in Fig. 4, deformation causes different changes inside a micro-pillar depending on the initial diameter. Micro-pillars favoring basal slips were not influenced by diameter changes except for a small localized deformation on the top of the pillar with a diameter of $9 \mu\text{m}$. Despite the remarkable stress burst and subsequent dislocation avalanches, no internal deformation after the compression was observed. This suggests the vanishing of dislocations at the free surface and the related occurrence of mechanical annealing in micro-pillars deformed in the basal slip system [40,41]. In contrast, a deformation behavior in micro-pillars favoring prismatic slips were significantly affected by the micro-pillars' diameter. The smallest micro-pillar was characterized by a uniform microstructure after deformation of up to 10 %. The increase in diameter to $6 \mu\text{m}$ resulted in a deformation localized to the top part of the micro-pillar. Moreover, localized deformation is even more pronounced in micro-pillars with a diameter of $9 \mu\text{m}$, where internal dislocation structures were formed. A tendency to form dislocation structures in different planes suggests a high contribution of screw dislocations and cross-slip during deformation in prismatic-oriented micro-pillars, leading to matrix rotation towards new basal-favored orientations [42,43]. The misorientation analysis performed along the yellow line in Fig. S2 presents a gradually changing orientation that excludes

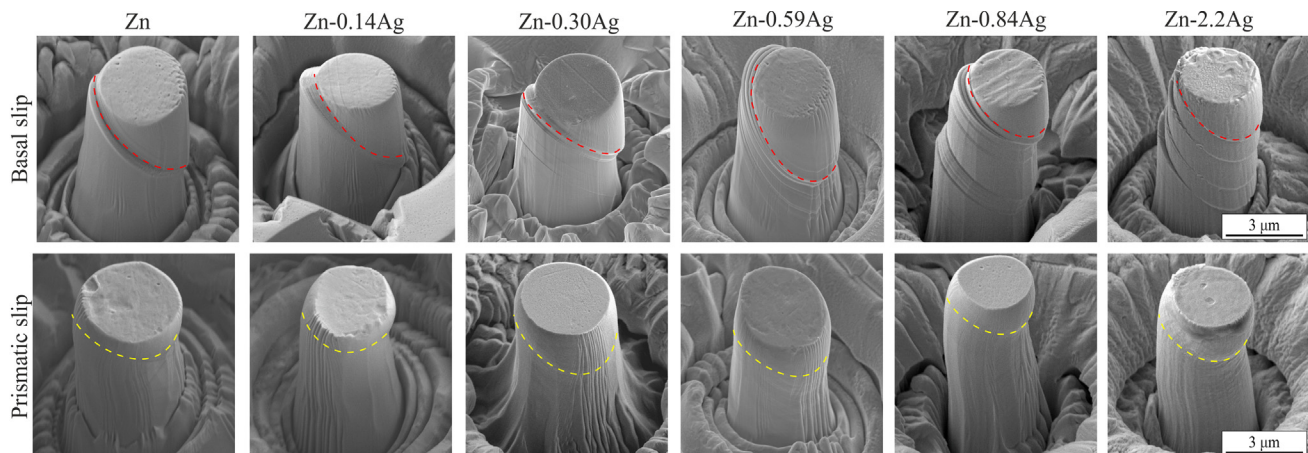


Fig. 8. SEM images of compressed micro-pillars, with up to 10 % deformation, in basal slip (top row) and prismatic slip (bottom row) systems at a strain rate of 10^{-3} s^{-1} .

possible twinning. The measured intragranular misorientation around $\langle 11\bar{2}0 \rangle$ axis (Taylor axis) implies the high activity of multiple pyramidal $\langle c + a \rangle$ slip systems. One variant of the pyramidal $\langle c + a \rangle$ slip system causes rotation about one variant of the Taylor $\langle 10\bar{1}0 \rangle$ axis. However, multiple activated pyramidal $\langle c + a \rangle$ variants will result in rotation about $\langle 11\bar{2}0 \rangle$ axis [44,45]. Moreover, the basal $\langle a \rangle$ slip may interact with the pyramidal $\langle c + a \rangle$ slip, creating the measured $\langle 11\bar{2}0 \rangle$ axis because both share the Taylor $\langle 10\bar{1}0 \rangle$ axes. Nevertheless, the presented results confirm the correctness of 3 μm micro-pillar preparation, especially for orientation analysis. Only the predicted slip system was activated in both analyzed orientations in the smallest micro-pillars, which is not always the case in HCP materials as showed here and in Mg alloys [46].

Apart from differences in the deformation behavior, micro-pillar diameter size mainly affects the pillars' measured strength. The obtained results indicate a strong size effect in compressed Zn micro-pillars that exhibit a CRSS of 11.3 MPa and 81.8 MPa for activating basal and prismatic slips, while CRSS for the same slip systems reported for bulk Zn single crystal are <0.5 MPa and ~3 MPa, respectively [39]. As shown in to Eq. (2), this study's generalized power-law exponents for the basal (m_B) and prismatic (m_P) slip systems are 0.77 and 0.17, respectively. The high m_B exponent value matches the reported exponent values (~0.6–1.0) in relatively soft face-centered cubic metals (FCC) [47–49] despite the considerably lower number of possible slip systems. Additionally, the low m_P value corresponds to BCC metals (~0.2–0.4) and their lower screw dislocations mobility [48]. Moreover, deformation through screw dislocations can be assumed as a significant mechanism in prismatic slip systems, due to the high tendency for cross-slips, which was confirmed during EBSD post-mortem analysis.

A prismatic to basal CRSS ratio is often used to determine the degree of deformation anisotropy. Therefore, this value was calculated for each pillar diameter. A decreasing tendency in $\text{CRSS}_P/\text{CRSS}_B$ ratio with decreasing pillar diameter was observed. For example, for pillars with a diameter of 3 μm , the ratio was 3.7:1, while for 9 μm pillars, the ratio was calculated to be 7.2:1. The $\text{CRSS}_P/\text{CRSS}_B$ ratio in bulk, coarse-grained Zn samples has been reported to be about 15:1 [38,39]. The observed tendency was that with reduced specific deformation size, deformation anisotropy decreased.

Unfortunately, the observed effect cannot be transferred directly to polycrystalline materials. However, the results presented here can help understand the high susceptibility to grain boundary sliding in fine-grained Zn alloy [50]. Grain refinement in Zn alloys acts as the primary factor activating grain boundary sliding in two ways. Firstly, grain refinement causes a characteristic reduction in grain boundary sliding shear stress, according to Eq. (4) [51]. Secondly, the CRSS in the preferred basal slip system increases. Both effects finally result in the activation of grain boundary sliding at the expense of dislocation slip deformation.

$$\dot{\epsilon} \propto \left(\frac{b}{d}\right)^p \left(\frac{\sigma}{G}\right)^n \quad (4)$$

where: b is the Burgers vector, d is the grain size, σ is the applied stress, p and n are the grain size and stress exponent, respectively.

4.2. The effect of Ag addition on CRSS and deformation behavior in 3 μm micro-pillars

The effect of Ag on solid solution strengthening presented in Fig. 7 generally agrees with Eq. (1). Except for values measured for pure Zn and Zn-0.14Ag, solid solution strengthening in basal

(σ_{sol_B}) and prismatic (σ_{sol_P}) slip systems can be described as follows:

$$\sigma_{\text{sol}_B} = 5.5 + 4.5^{-\frac{1}{2}} \cdot c^{\frac{1}{2}} \quad (5)$$

$$\sigma_{\text{sol}_P} = 76.7 + 8.3^{-\frac{1}{2}} \cdot c^{\frac{1}{2}} \quad (6)$$

the measured strengthening coefficient k_{sol} in basal and prismatic slip systems differs from the value measured in our previous studies, where k_{sol} equaled 6.6 MPa (at. %)^{-1/2} [20]. The observed differences result from the isolated slip deformation in micro-pillar compression in contrast to complex deformation in polycrystalline macroscopic bulk samples investigated previously. According to Eq. (5) and Eq. (6), the CRSS value for pure Zn should equal 5.5 MPa and 76.7 MPa instead of 26.6 MPa and 98.9 MPa in the basal and prismatic slip systems, respectively.

These results imply that besides solid-solution strengthening, another phenomenon has to be responsible for the observed unexpected behavior of pure Zn. The dislocation density effect tends to play a significant role in micro-mechanical tests. Firstly, high-temperature annealing significantly reduces the dislocation density in a polycrystalline sample. Early studies have reported exceptionally low dislocation densities of approx. 10^7 – 10^{10} m^{-2} in pure Zn [52–54]. Secondly, micro-pillar FIB milling created a new free surface, promoting further dislocation annihilation. As reported for copper, the dislocation density in micro-pillars can be one order of magnitude smaller than in bulk single crystals [55]. Consequently, the dislocation density in the fabricated Zn micro-pillars might be even smaller than mentioned above. It indicates that pure Zn micro-pillars can be considered as dislocation-free. Moreover, according to early reports, the dislocation density after high-temperature annealing significantly depends on the amount of solutes and impurities [56,57]. Regardless of the investigated material, reducing the dislocation density in micro-crystals below a critical value increases shear stress when stochastic effects occur [43]. Following this theory, a higher CRSS value and its deviation in both slip systems in pure Zn indicates the critically low dislocation density or lack of dislocations in the tested micro-pillars. Therefore, it is believed that the samples with Ag additions initially had a higher dislocation density than pure Zn, which resulted in more predictable deformation behavior of the prepared micro-pillars instead of high-stress, stochastic dislocation nucleation-based deformation. It is likely, that in the Zn-Ag micro-pillars dislocations are generated and multiplied into the slip planes based on the Frank-Read sources randomly distributed in the micro-pillars volume. They may facilitate initial slip activation compared to pure Zn micro-pillars, and further contribute to dislocation density increase, as they are work-hardened [58]. The stress-strain curves showing the differences in the mechanical response of pure Zn and Zn-Ag alloys are presented in Fig. S1 in [supplementary materials](#). As can be seen, compression of pure Zn micropillars in basal slip-favored orientation resulted in achieving varied peak flow stresses ranging from about 40 MPa to 230 MPa. The large spread of these values is related to a stochastic behavior during plastic deformation of dislocation-free micro-pillars. It is worth mentioning that the highest observed yield strength equal to 230 MPa is a significant fraction of the theoretical strength, which is 10 % of the Young's modulus typically. Depending on the Zn crystal orientation, Young's modulus varies from ~36 GPa in the (0001) direction to ~126 GPa in the $\langle 10\bar{1}0 \rangle$ direction [59]. Based on the measured effect of Ag content on the deformation curves and lack in stored deformation, dislocation starvation is the governing deformation mechanism in 3 μm micro-pillars favorably oriented for basal slips produced in Zn alloys with Ag additions up to 0.30 at. %. It means that dislocations vanish from the free sur-

face faster than they multiply inside the micro-pillars, so higher stresses are required to nucleate enough dislocations to compensate for their disappearance on the free surface and allow for plastic deformation. At the beginning of deformation, dislocations have to be generated, which creates high peak stress, however, afterwards the dislocations easily escape the crystal. This results in a significant drop in stress and lack of strain hardening [60]. In contrast, a slightly higher strengthening effect occurs in the basal slip system in the Zn-2.21Ag alloy, resulting from forest strengthening controlled by a lower recovery rate, higher dislocation density, and higher dislocation source density [43]. Post-deformation SEM imaging confirmed a lack of hardening in pure Zn demonstrated by highly localized deformation. Once deformation is activated in a particular slip plane, it can constantly reoccur in pure Zn due to dislocation annihilation on a free surface. The absence of a sufficient amount of effective obstacles for dislocation glide leads to localized slip and consequently induces strain softening. In Zn-2.21Ag pillars, slip deformation produces a high dislocation density on the activated slip plane, impeding further deformation through this plane. This can be related to the interaction between Ag solute atoms and the initial dislocation structure present in the micro-pillar and multiplying during deformation.

The increased amount of Ag atoms in the Zn crystal lattice leads to increased shear strength due to more obstacles hindering the gliding of the multiplied dislocations. In the case of a prismatic slip, the CRSS_p value remains almost unaffected for pure Zn compared to the lowest Ag content (0.14 at. %), while a further increase in Ag content contributes to the prominent increase in CRSS_p. It suggests that the stress required for dislocation slip is at a similar level as for dislocation nucleation. In this case, low dislocation densities slightly affect the CRSS_p in pure Zn. The results presented in Fig. 6b indicate that solid solution strengthening acts here as a prevailing source of the strengthening process during deformation [61]. This is in contrast to the effect of Zn and Al in Mg alloys, which results in solute softening with increasing solute content in the prismatic slip system. The role of these solute atoms is explained by facilitating dislocation cross slipping and improving dislocations' ability to form jog-pairs [62,63]. Ag may have an opposite effect in Zn because Ag atoms are smaller than Zn atoms, while Al and Zn atoms are bigger than Mg ones. Therefore, it may produce different strain fields around the solute atoms in the lattice that eventually interact with the dislocations. In addition, the opposite effect in Mg-based alloys may come from different *c/a* ratios of Zn and Mg and the effect of solute atoms on this lattice parameter: Ag decreases the *c/a* ratio in Zn, while Al increases *c/a* in Mg and Zn does not affect *c/a* [19,64].

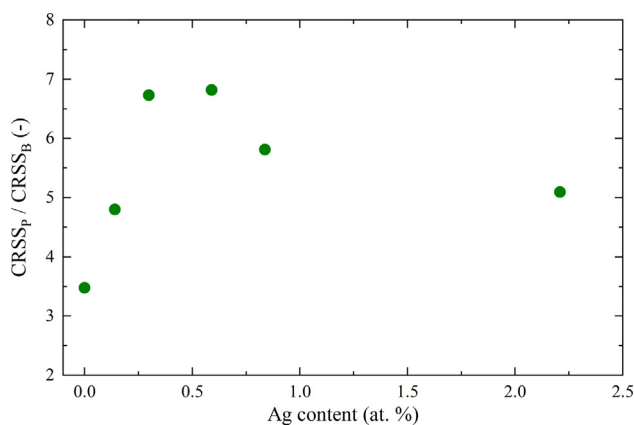


Fig. 9. The effect of Ag content on the prismatic to basal slip CRSS ratio in 3 μm micro-pillars.

The dependence of the CRSS_p/CRSS_b ratio on the Ag content does not follow the expected reduction within the investigated range of Ag concentration (Fig. 9). Instead, two ranges can be distinguished. In the first one, for Zn-Ag micro-pillars with Ag concentrations below 0.5 at. %, the strengthening mechanism was disrupted by the dislocation starvation effect in the basal slip system, while above this concentration, i.e. in the second range, the strengthening was governed mainly through the solid solution effect. The decrease in the CRSS_p/CRSS_b ratio from 7 for Zn-0.59Ag to 5 for Zn-2.21Ag was recorded. It may indicate that in Zn-Ag samples not suffering from a critically low dislocation density, Ag would positively affect the reduction of plastic anisotropy in the mechanical response of Zn. Nevertheless, this relation requires more studies, also for other non-basal slip deformation modes.

5. Conclusions

In this work, the experimental methodology based on *in situ* micro-pillar compression was used to assess the size effect in pure Zn and to characterize the influence of Ag solute content on the CRSS for the basal and prismatic *<a>* slip systems at different strain rates. The main findings of the proposed *in situ* measurements can be summarized as follows:

1. Both yield stress and strain hardening depend on the micro-pillar diameter size within a 3 μm to 9 μm range. Micro-pillar diameter reduction resulted in a CRSS increase in both slip systems. The CRSS in the basal slip system changed from 11.3 MPa to 26.6 MPa for 9 μm and 3 μm pillars, respectively. In the prismatic slip system, the size effect was less pronounced, and the CRSS_p changed from 81.8 MPa to 99.1 MPa within the same pillar size range.
2. The measurements performed at strain rates from 10⁻⁴ s⁻¹ to 10⁻² s⁻¹ proved the negligible effect of strain rate on dislocation-based deformation mechanisms. It demonstrates the non-dislocation origin of high strain rate sensitivity observed in polycrystalline Zn alloys.
3. The extraordinarily high CRSS_b values in pure Zn and the Zn-0.14Ag alloy compared to the solid solution strengthening model is most likely attributed to the critically low dislocation density in the fabricated micro-pillars. Therefore, deformation requires the activation of dislocation sources, which lead to stochastic dislocation creation and subsequent dislocation avalanches. Furthermore, with increasing Ag content, the dislocation density in the prepared micro-pillars increases, causing dislocation-moderated deformation.
4. Ag atoms are generally more effective in increasing the CRSS for prismatic slipping than basal slipping. The increase from 26.6 MPa to 37.0 MPa (by ~ 40 %) in the basal slip and from 99.1 MPa to 188.4 MPa (by ~ 104 %) in the prismatic slip for pure Zn and Zn-2.21Ag, respectively, was observed. The solid solution strengthening coefficient for basal and prismatic slip systems was calculated to be 4.5 MPa·(at.%)^{-1/2} and 8.3 MPa·(at.%)^{-1/2}, respectively.
5. The CRSS_p/CRSS_b ratio in pure Zn crystal decreased with the decrease in micro-pillar diameter. The effect of Ag solute content on the variation of Zn plastic anisotropy is ambiguous and should be considered only for Ag concentrations above 0.5 at. %. The overall 28 % decrease in the CRSS_p/CRSS_b ratio was observed with the increase in Ag content from 0.59 at. % to 2.21 at. % in Zn. Micro-pillars with lower Ag concentrations and low dislocation densities relevant for activating the basal slip have plastic anisotropy compared to pure Zn.

Data availability

Data will be made available on request.

Declaration of Competing Interest

The authors declare the following financial interests/personal relationships which may be considered as potential competing interests: Wiktor Bednarczyk reports financial support was provided by National Science Centre Poland. Krzysztof Wiecezrak reports financial support was provided by European Union. Johann Michler is the member of Materials & Design International Editorial Board.

Acknowledgments

This work was supported by the National Science Centre, Poland [Grant number: ETIUDA 2019/32/T/ST5/00550] (W.B.). K.W. was supported by the EMPAPOSTDOCS-II program that has received funding from the European Union's Horizon 2020 research and innovation program under the Marie Skłodowska-Curie grant agreement number 754364. W. Bednarczyk and M. Wątroba contributed equally to this work.

Appendix A. Supplementary material

Supplementary data to this article can be found online at <https://doi.org/10.1016/j.matdes.2023.111897>.

References

- [1] H. Kabir, K. Munir, C. Wen, Y. Li, Recent research and progress of biodegradable zinc alloys and composites for biomedical applications: biomechanical and biocorrosion perspectives, *Bioact. Mater.* 6 (2021) 836–879, <https://doi.org/10.1016/j.bioactmat.2020.09.013>.
- [2] H. Yang, B. Jia, Z. Zhang, X. Qu, G. Li, W. Lin, D. Zhu, K. Dai, Y. Zheng, Alloying design of biodegradable zinc as promising bone implants for load-bearing applications, *Nat. Commun.* 11 (2020) 1–16, <https://doi.org/10.1038/s41467-019-14153-7>.
- [3] M. Wątroba, W. Bednarczyk, J. Kawałko, S. Lech, K. Wiecezrak, T.G. Langdon, P. Bała, A novel high-strength Zn-3Ag-0.5Mg alloy processed by hot extrusion, cold rolling, or high-pressure torsion, *Metall. Mater. Trans. A* 51 (2020) 3335–3348, <https://doi.org/10.1007/s11661-020-05797-y>.
- [4] X. Xiao, E. Liu, J. Shao, S. Ge, Advances on biodegradable zinc-silver-based alloys for biomedical applications, *J. Appl. Biomater. Funct. Mater.* 19 (2021), <https://doi.org/10.1177/22808000211062407>.
- [5] M. Wątroba, W. Bednarczyk, P.K. Szewczyk, J. Kawałko, K. Mech, A. Grünwald, I. Unalan, N. Taccardi, G. Boelter, M. Banzhaf, C. Hain, P. Bała, A.R. Boccaccini, In vitro cytocompatibility and antibacterial studies on biodegradable Zn alloys supplemented by a critical assessment of direct contact cytotoxicity assay, *J. Biomed. Mater. Res. Part B Appl. Biomater.* (2022) 1–20, <https://doi.org/10.1002/jbm.b.35147>.
- [6] E. Mostaed, M. Sikora-Jasinska, M.S. Ardakani, A. Mostaed, I.M. Reaney, J. Goldman, J.W. Drelich, Towards revealing key factors in mechanical instability of bioabsorbable Zn-based alloys for intended vascular stenting, *Acta Biomater.* 105 (2020) 319–335, <https://doi.org/10.1016/j.actbio.2020.01.028>.
- [7] M. Wątroba, K. Mech, W. Bednarczyk, J. Kawałko, M. Marciszko-Wiąckowska, M. Marzec, D.E.T. Shepherd, P. Bała, Long-term in vitro corrosion behavior of Zn-3Ag and Zn-3Ag-0.5Mg alloys considered for biodegradable implant applications, *Mater. Des.* 213 (2022), <https://doi.org/10.1016/j.matdes.2021.110289>.
- [8] P.G. Partridge, The crystallography and deformation modes of hexagonal close-packed metals, *Metall. Rev.* 12 (1967) 169–194, <https://doi.org/10.1179/mtlr.1967.12.1.169>.
- [9] D.H. Lassila, M.M. LeBlanc, J.N. Florando, Zinc single-crystal deformation experiments using a “6 degrees of freedom” apparatus, *Metall. Mater. Trans. A* 38 A (2007) 2024–2032, <https://doi.org/10.1007/s11661-007-9202-x>.
- [10] R. Parisot, S. Forest, A. Pineau, F. Grillon, X. Demonet, J.-M. Maitigne, Deformation and damage mechanisms of zinc coatings on hot-dip galvanized steel sheets: Part I. Deformation modes, *Metall. Mater. Trans. A* 35 (2004) 797–811, <https://doi.org/10.1007/s11661-004-0007-x>.
- [11] S. Liu, D. Kent, H. Zhan, N. Doan, M. Dargusch, G. Wang, Dynamic recrystallization of pure zinc during high strain-rate compression at ambient temperature, *Mater. Sci. Eng. A* 784 (2020), <https://doi.org/10.1016/j.msea.2020.139325>.
- [12] R.E. Cooper, J. Washburn, Stress-induced movement of twin boundaries in zinc, *Acta Metall.* 15 (1967) 639–647, [https://doi.org/10.1016/0001-6160\(67\)90107-1](https://doi.org/10.1016/0001-6160(67)90107-1).
- [13] R.L. Bell, R.W. Cahn, The dynamics of twinning and the interrelation of slip and twinning in zinc crystals, *Proc. R. Soc. London. Ser. A. Math. Phys. Sci.* 239 (1957) 494–521, <https://doi.org/10.1098/rspa.1957.0058>.
- [14] M.J.J. Philippe, F. Wagner, F.E.E. Mellab, C. Esling, J. Wegria, Modelling of texture evolution for materials of hexagonal symmetry—I. Application to zinc alloys, *Acta Metall. Mater.* 42 (1994) 239–250, [https://doi.org/10.1016/0956-7151\(94\)90066-3](https://doi.org/10.1016/0956-7151(94)90066-3).
- [15] S. Furukawa, K. Oka, M. Tsushida, H. Kitahara, S. Ando, Orientation dependence on bending deformation behavior of pure zinc single crystals, *Mater. Trans.* 63 (2022) MT-M2021253, doi: 10.2320/matertrans.MT-M2021253.
- [16] J.Y. Wang, N. Li, R. Alizadeh, M.A.A. Monclús, Y.W.W. Cui, J.M.M. Molina-Aldareguia, J. Llorca, Effect of solute content and temperature on the deformation mechanisms and critical resolved shear stress in Mg-Al and Mg-Zn alloys, *Acta Mater.* 170 (2019) 155–165, <https://doi.org/10.1016/j.actamat.2019.03.027>.
- [17] N. Li, C. Wang, M.A. Monclús, L. Yang, J.M. Molina-Aldareguia, Solid solution and precipitation strengthening effects in basal slip, extension twinning and pyramidal slip in Mg-Zn alloys, *Acta Mater.* 221 (2021), <https://doi.org/10.1016/j.actamat.2021.117374>.
- [18] T. Tsuru, D.C. Chrzan, Effect of solute atoms on dislocation motion in Mg: an electronic structure perspective, *Sci. Rep.* 5 (2015) 8793, <https://doi.org/10.1038/srep08793>.
- [19] C. Chen, S. Fan, J. Niu, H. Huang, Z. Jin, L. Kong, D. Zhu, G. Yuan, Alloying design strategy for biodegradable zinc alloys based on first-principles study of solid solution strengthening, *Mater. Des.* 204 (2021), <https://doi.org/10.1016/j.matdes.2021.109676>.
- [20] W. Bednarczyk, J. Kawałko, B. Rutkowski, M. Wątroba, N. Gao, M.J. Starink, P. Bała, T.G. Langdon, Abnormal grain growth in a Zn-0.8Ag alloy after processing by high-pressure torsion, *Acta Mater.* 207 (2021), <https://doi.org/10.1016/j.actamat.2021.116667>.
- [21] L.A. Gypen, A. Deruyttere, Multi-component solid solution hardening - Part 1 Proposed model, *J. Mater. Sci.* 12 (1977) 1028–1033, <https://doi.org/10.1007/BF00540987>.
- [22] L.A. Gypen, A. Deruyttere, Multi-component solid solution hardening - Part 2 Agreement with experimental results, *J. Mater. Sci.* 12 (1977) 1034–1038, <https://doi.org/10.1007/BF00540988>.
- [23] M. Sikora-Jasinska, E. Mostaed, A. Mostaed, R. Beanland, D. Mantovani, M. Vedani, Fabrication, mechanical properties and in vitro degradation behavior of newly developed Zn-Ag alloys for degradable implant applications, *Mater. Sci. Eng. C* 77 (2017) 1170–1181, <https://doi.org/10.1016/j.msec.2017.04.023>.
- [24] Z. Liu, D. Qiu, F. Wang, J.A. Taylor, M. Zhang, The grain refining mechanism of cast zinc through silver inoculation, *Acta Mater.* 79 (2014) 315–326, <https://doi.org/10.1016/j.actamat.2014.07.026>.
- [25] S. Shahbeyk, G.Z. Voyiadjijs, V. Habibi, S.H. Astaneh, M. Yaghoobi, Review of size effects during micropillar compression test: experiments and atomistic simulations, *Crystals* 9 (2019), <https://doi.org/10.3390/cryst9110591>.
- [26] M.D. Uchic, P.A. Shade, D.M. Dimiduk, Plasticity of micrometer-scale single crystals in compression, *Annu. Rev. Mat. Res.* 39 (2009) 361–386, <https://doi.org/10.1146/annurev-matsci-082908-145422>.
- [27] P.D. Ispánovity, D. Ugi, G. Péterffy, M. Knappek, S. Kalácska, D. Tüzes, Z. Dankházi, K. Máthi, F. Chmelfik, I. Groma, Dislocation avalanches are like earthquakes on the micron scale, *Nat. Commun.* 13 (2022) 1975, <https://doi.org/10.1038/s41467-022-29044-7>.
- [28] R. Soler, J.M. Wheeler, H.J. Chang, J. Segurado, J. Michler, J. Llorca, J.M. Molina-Aldareguia, Understanding size effects on the strength of single crystals through high-temperature micropillar compression, *Acta Mater.* 81 (2014) 50–57, <https://doi.org/10.1016/j.actamat.2014.08.007>.
- [29] C.M. Byer, B. Li, B. Cao, K.T. Ramesh, Microcompression of single-crystal magnesium, *Scr. Mater.* 62 (2010) 536–539, <https://doi.org/10.1016/j.scriptamat.2009.12.017>.
- [30] Q. Yu, R.K. Mishra, A.M. Minor, The effect of size on the deformation twinning behavior in hexagonal close-packed Ti and Mg, *JOM* 64 (2012) 1235–1240, <https://doi.org/10.1007/s11837-012-0437-7>.
- [31] J. Hütsch, E.T. Lilleodden, The influence of focused-ion beam preparation technique on microcompression investigations: Lathe vs. annular milling, *Scr. Mater.* 77 (2014) 49–51, <https://doi.org/10.1016/j.scriptamat.2014.01.016>.
- [32] J.A. El-Awady, C. Woodward, D.M. Dimiduk, N.M. Ghoniem, Effects of focused ion beam induced damage on the plasticity of micropillars, *Phys. Rev. B* 80 (2009), <https://doi.org/10.1103/PhysRevB.80.104104>.
- [33] J. Wang, M. Ramajayam, E. Charrault, N. Stanford, Quantification of precipitate hardening of twin nucleation and growth in Mg and Mg-5Zn using micro-pillar compression, *Acta Mater.* 163 (2019) 68–77, <https://doi.org/10.1016/j.actamat.2018.10.009>.
- [34] M. Chen, J. Wehrs, A.S. Sologubenko, J. Rabier, J. Michler, J.M. Wheeler, Size-dependent plasticity and activation parameters of lithographically-produced silicon micropillars, *Mater. Des.* 189 (2020), <https://doi.org/10.1016/j.matdes.2020.108506>.
- [35] Y. Xiao, R. Kozak, M.J.R. Haché, W. Steurer, R. Spolenak, J.M. Wheeler, Y. Zou, Micro-compression studies of face-centered cubic and body-centered cubic high-entropy alloys: size-dependent strength, strain rate sensitivity, and activation volumes, *Mater. Sci. Eng. A* 790 (2020), <https://doi.org/10.1016/j.msea.2020.139429>.

- [36] M. Wątroba, W. Bednarczyk, J. Kawałko, P. Bała, Fine-tuning of mechanical properties in a Zn–Ag–Mg alloy via cold plastic deformation process and post-deformation annealing, *Bioact. Mater.* 6 (2021) 3424–3436, <https://doi.org/10.1016/j.bioactmat.2021.03.017>.
- [37] W. Bednarczyk, M. Wątroba, J. Kawałko, P. Bała, Determination of room-temperature superplastic asymmetry and anisotropy of Zn–0.8Ag alloy processed by ECAP, *Mater. Sci. Eng. A* 759 (2019) 55–58, <https://doi.org/10.1016/j.msea.2019.05.029>.
- [38] J.J. Fundenberger, M.J. Philippe, F. Wagner, C. Esling, Modelling and prediction of mechanical properties for materials with hexagonal symmetry (zinc, titanium and zirconium alloys), *Acta Mater.* 45 (1997) 4041–4055, [https://doi.org/10.1016/S1359-6454\(97\)00099-2](https://doi.org/10.1016/S1359-6454(97)00099-2).
- [39] L. Cauvin, B. Raghavan, S. Bouvier, X. Wang, F. Meraghni, Multi-scale investigation of highly anisotropic zinc alloys using crystal plasticity and inverse analysis, *Mater. Sci. Eng. A* 729 (2018) 106–118, <https://doi.org/10.1016/j.msea.2018.05.038>.
- [40] J.Y. Zhang, G. Liu, J. Sun, Strain rate effects on the mechanical response in multi- and single-crystalline Cu micropillars: grain boundary effects, *Int. J. Plast.* 50 (2013) 1–17, <https://doi.org/10.1016/j.ijplas.2013.03.009>.
- [41] P. Zhang, O.U. Salman, J.Y. Zhang, G. Liu, J. Weiss, L. Truskinovsky, J. Sun, G. Liu, Taming intermittent plasticity at small scales, *Acta Mater.* 128 (2017) 351–364, <https://doi.org/10.1016/j.actamat.2017.02.039>.
- [42] J.A. El-Awady, M. Wen, N.M. Ghoniem, The role of the weakest-link mechanism in controlling the plasticity of micropillars, *J. Mech. Phys. Solids* 57 (2009) 32–50, <https://doi.org/10.1016/j.jmps.2008.10.004>.
- [43] J.A. El-Awady, Unravelling the physics of size-dependent dislocation-mediated plasticity, *Nat. Commun.* 6 (2015) 5926, <https://doi.org/10.1038/ncomms6926>.
- [44] Y.B. Chun, M. Battaini, C.H.J. Davies, S.K. Hwang, Distribution characteristics of in-grain misorientation axes in cold-rolled commercially pure titanium and their correlation with active slip modes, *Metall. Mater. Trans. A* 41 (2010) 3473–3487, <https://doi.org/10.1007/s11661-010-0410-4>.
- [45] J.P. Hadorn, K. Hantzsche, S. Yi, J.A.N. Bohlen, D. Letzig, J.A. Wollmershauser, S. R. Agnew, Role of solute in the texture modification during hot deformation of Mg–Rare Earth alloys, *Metall. Mater. Trans. A* 43 (2012) 1347–1362, <https://doi.org/10.1007/s11661-011-0923-5>.
- [46] J. Wang, Y. Chen, Z. Chen, J. Llorca, X. Zeng, Deformation mechanisms of Mg–Ca–Zn alloys studied by means of micropillar compression tests, *Acta Mater.* 217 (2021), <https://doi.org/10.1016/j.actamat.2021.117151> 117151.
- [47] Z. Chen, H. Inui, Micropillar compression deformation of single crystals of Fe₃Ge with the L1₂ structure, *Acta Mater.* 208 (2021), <https://doi.org/10.1016/j.actamat.2021.116779> 116779.
- [48] R. Soler, J.M. Molina-Aldareguia, J. Segurado, J. Llorca, R.I. Merino, V.M. Orera, Micropillar compression of LiF [111] single crystals: effect of size, ion irradiation and misorientation, *Int. J. Plast.* 36 (2012) 50–63, <https://doi.org/10.1016/j.ijplas.2012.03.005>.
- [49] J. Li, J. Liu, Z. Guan, G. Yao, C. Linsley, B.M. Wu, J.M. Yang, Fabrication and characterization of bioresorbable zinc/WC nanocomposite springs for short bowel syndrome treatment, *Mater. Lett.* 280 (2020), <https://doi.org/10.1016/j.matlet.2020.128577> 128577.
- [50] W. Bednarczyk, M. Wątroba, J. Kawałko, P. Bała, Can zinc alloys be strengthened by grain refinement? A critical evaluation of the processing of low-alloyed binary zinc alloys using ECAP, *Mater. Sci. Eng. A* 748 (2019) 357–366, <https://doi.org/10.1016/j.msea.2019.01.117>.
- [51] T.G. Langdon, Grain boundary sliding revisited: developments in sliding over four decades, *J. Mater. Sci.* 41 (2006) 597–609, <https://doi.org/10.1007/s10853-006-6476-0>.
- [52] D.P. Pope, T.J. Vreeland, D.S. Wood, The Mobility of Edge Dislocations in the Basal Slip System of Zinc, California Institute of Technology, 1967, <https://resolver.caltech.edu/CaltechETD:etd-10042002-081427>.
- [53] K.H. Adams, Dislocation Mobility and Density in Zinc Single Crystals, California Institute of Technology, 1965, doi: 10.7907/SYCE-8B03.
- [54] N. Nagata, T. Vreeland, Basal dislocation interactions with a forest of non-basal dislocations in zinc, *Phil. Mag.* 25 (1972) 1137–1150, <https://doi.org/10.1080/14786437208226857>.
- [55] S. Kalácska, Z. Dankházi, G. Zilahi, X. Maeder, J. Michler, P.D. Ispánovity, I. Groma, Investigation of geometrically necessary dislocation structures in compressed Cu micropillars by 3-dimensional HR-EBSD, *Mater. Sci. Eng. A* 770 (2020), <https://doi.org/10.1016/j.msea.2019.138499>.
- [56] F.W. Young, J.R. Savage, Growth of copper crystals of low dislocation density, *J. Appl. Phys.* 35 (1964) 1917–1924, <https://doi.org/10.1063/1.1713770>.
- [57] Y. Sun, L. Peng, G. Huang, H. Xie, X. Mi, X. Liu, Effects of Mg addition on the microstructure and softening resistance of Cu–Cr alloys, *Mater. Sci. Eng. A* 776 (2020), <https://doi.org/10.1016/j.msea.2020.139009> 139009.
- [58] G.R. Huang, J.C. Huang, W.Y. Tsai, Origin of sample size effect: stochastic dislocation formation in crystalline metals at small scales, *Sci. Rep.* 6 (2016) 6–11, <https://doi.org/10.1038/srep39242>.
- [59] D. Tromans, Elastic anisotropy of HCP metal crystals and polycrystals, *Int. J. Res. Rev. Appl. Sci.* 6 (2011) 462–483, [https://doi.org/10.1016/0039-6028\(86\)90086-5](https://doi.org/10.1016/0039-6028(86)90086-5).
- [60] A.A. Benzerga, On the effects of dislocation density on micropillar strength, *Mater. Res. Soc. Symp. Proc.* 1185 (2009) 51–62, <https://doi.org/10.1557/proc-1185-ii05-07>.
- [61] M. Mlikota, S. Schmauder, On the critical resolved shear stress and its importance in the fatigue performance of steels and other metals with different crystallographic structures, *Metals (Basel)* 8 (2018) 883, <https://doi.org/10.3390/met8110883>.
- [62] N. Stanford, M.R. Barnett, Solute strengthening of prismatic slip, basal slip and 1012 twinning in Mg and Mg–Zn binary alloys, *Int. J. Plast.* 47 (2013) 165–181, <https://doi.org/10.1016/j.ijplas.2013.01.012>.
- [63] A. Akhtar, E. Teghtsoonian, Solid solution strengthening of magnesium single crystals-ii the effect of solute on the ease of prismatic slip, *Acta Metall.* 17 (1969) 1351–1356, [https://doi.org/10.1016/0001-6160\(69\)90152-7](https://doi.org/10.1016/0001-6160(69)90152-7).
- [64] J.S. Park, Y.W. Chang, The effect of alloying elements on the c/a ratio of magnesium binary alloys, *Adv. Mater. Res.* 26–28 (2007) 95–98, <https://doi.org/10.4028/www.scientific.net/amr.26-28.95>.